



Modeling Commercial-Scale CO₂ Storage in the Gas Hydrate Stability Zone with PFLOTRAN v6.0

Michael Nole¹, Jonah Bartrand¹, Fawz Naim², and Glenn Hammond¹

¹Pacific Northwest National Laboratory, Richland, 99354, USA

5 ²Ohio State University, Columbus, 43210, USA

Correspondence to: Michael Nole (michael.nole@pnnl.gov)

Abstract

Safe and secure carbon dioxide (CO₂) storage is likely to be critical for mitigating some of the most dangerous effects of climate change. In the last decade, there has been a significant increase in activity associated with reservoir characterization and site selection for large-scale CO₂ storage projects across the globe. These prospective storage sites tend to be terrestrial sites selected for their optimal structural, petrophysical, and geochemical trapping potential. However, it has also been suggested that storing CO₂ in reservoirs within the gas hydrate stability zone (GHSZ), characterized by high pressures and low temperatures (e.g., Arctic or marine environments), could provide natural thermodynamic and solubility barriers to gas leakage. Evaluating the prospect of commercial-scale, long-term storage of CO₂ in the GHSZ requires reservoir-scale modelling capabilities designed to account for the unique physics and thermodynamics associated with these systems. We have developed the HYDRATE flow mode and accompanying fully implicit parallel well model in the massively parallel subsurface flow and reactive transport simulator PFLOTRAN to model CO₂ injection into the marine GHSZ. We have applied these capabilities to a set of CO₂ injection scenarios designed to reveal the challenges and opportunities for commercial-scale CO₂ storage in the GHSZ.

20 1 Introduction

Large-scale deployment of carbon capture and storage (CCS) projects is likely to be critical for constraining future global temperature increase due to climate change, yet major uncertainties exist regarding potential injectivity of CO₂ in subsurface reservoirs (Lane et al., 2021). Evaluating terrestrial CO₂ storage sites for long-term sequestration requires synthesizing sophisticated laboratory, field, and modelling tools to assess the CO₂ trapping potential of a prospective subsurface reservoir during a large-scale injection over a significant post-injection performance period. CO₂ trapping in terrestrial sequestration involves potentially both physical and chemical trapping mechanisms which include structural, solubility, capillary, and mineralization trapping (Al Hameli et al., 2022). Currently, large-scale carbon capture and storage (CCS) projects around the globe are each storing over 400,000 metric tons (Mt) of CO₂ annually (Snæbjörnsdóttir et al., 2020); the U.S. Department of Energy's CarbonSAFE initiative aims to develop CO₂ storage complexes across the U.S. that would be capable of storing total



30 volumes exceeding 50 million metric tons (MMt) of CO₂ each (Sullivan et al., 2020). To achieve this vision, a diverse set of potential reservoir host rocks and environments is being considered. This includes speculation about the feasibility of offshore CO₂ sequestration and mineralization, such as in Cascadia Basin basalts offshore the U.S. Pacific Northwest (Goldberg et al., 2018). Shallow sub-sea environments are not only isolated from the atmosphere by a large water body, but they can also exist in a unique pressure and temperature regime conducive for forming gas hydrate.

35 Gas hydrate is a solid-phase, non-stoichiometric mixture of low molecular weight gas molecules occupying free spaces in a solid water lattice. Hydrates of several different gases occur abundantly in nature, but since the hydrate phase is only stable at high pressures and low temperatures it is only found naturally on Earth in the pore space of soils in either permafrost or sub-sea environments. Methane hydrate is of interest for its potential as a natural gas energy resource (Collett, 2000; Oyama et al., 40 2017; Singh et al., 2022), for its potential role in global carbon cycling as the climate changes (Ruppel and Kessler, 2017), and for its role as a geohazard (Zander et al., 2018; Kaminski et al., 2020). On the other hand, carbon dioxide (CO₂) hydrate, which forms at similar pressures and temperatures as methane hydrate, is increasingly being explored as a potential means to permanently sequester CO₂ as a climate change mitigation solution that comes with additional safety factors beyond those typically encountered in terrestrial CO₂ sequestration scenarios. These include the fact that it is immobile in sediment pore 45 space, which adds a thermodynamic barrier to gas escape, and the presence of a significant ocean sink in marine environments which isolates CO₂ from release into the atmosphere (Tohidi et al., 2010). An added benefit of CO₂ injection into the methane hydrate stability zone is that CO₂ hydrate is typically more thermodynamically favourable than methane hydrate, meaning it could theoretically be possible to use CO₂ to kick out methane from the hydrate phase, thus sequestering CO₂ while producing natural gas from a methane hydrate deposit (Koh et al., 2016).

50 CO₂ sequestration in gas hydrate form can only occur in a finite bounded temperature and pressure range. In terms of a soil column, there exists a depth-bounded gas hydrate stability zone (GHSZ) in the subsurface in which hydrate can form. In a marine environment, the GHSZ typically begins several meters above the seafloor, but hydrate does not form freely in the water column (except for, e.g., as a gas bubble crust [Fu et al., 2021]) because the guest molecule gas (e.g., CO₂) typically 55 cannot become concentrated enough in the water to do so. Therefore, the seafloor is typically the shallowest extent of hydrate formation in marine systems. Relative to deeper sediments, this point usually represents a minimum temperature and pressure. Working downward through the GHSZ, pressure increases roughly hydrostatically and temperature increases along a geothermal gradient. Increases in pressure stabilize hydrate, while increases in temperature destabilize hydrate. The geothermal temperature change effect on hydrate stability outweighs the hydrostatic pressure change effect, so there exists a depth below 60 the seafloor where the temperature is too high to form hydrate, known as the base of the gas hydrate stability zone (BHSZ). Overall, the specific thickness of the bulk GHSZ is dependent on pressure, temperature, porewater salinity and gas composition (Sloan and Koh, 2007).



65 For a potential host reservoir within the GHSZ, the long-term CO₂ storage potential of the reservoir would consider the thermodynamic trapping mechanism of solid gas hydrate formation in addition to traditional trapping mechanisms. Several experimental studies have demonstrated the process of CO₂ trapping and hydrate conversion in the GHSZ at the lab-scale, demonstrating how conversion of CO₂ into a solid phase adds an additional safety factor (Gauteplass et al., 2020; Rehman et al., 2021). An experimental study of layered sediments using different injection strategies demonstrated the need to consider thermal management when designing a CO₂ injection in the GHSZ and suggested multilateral perforated horizontal wells may
70 achieve the most optimal CO₂ conversion efficiency (Pang et al., 2024). However, reservoir-scale modelling studies of the transport and thermodynamic phenomena associated with injection of CO₂ in commercial volumes into the GHSZ are lacking.

We present several new capabilities developed in the open source, massively parallel multiphase flow and reactive transport simulator PFLOTTRAN (Hammond et al., 2014) to model reservoir-scale injection of CO₂ in the GHSZ. We have extended
75 PFLOTTRAN's HYDRATE mode capabilities to model free-phase CO₂ flow properties and CO₂ hydrate phase behaviour. Additionally, we introduce a fully coupled parallel well model that can be used to model CO₂ injection into heterogeneous media and can adapt to changes in flow properties associated with hydrate formation in the vicinity of the wellbore. Finally, we add a new fully coupled salt mass balance to consider salinity and salt precipitation effects in the GHSZ. We demonstrate these capabilities on a series of test problems designed to elucidate the challenges and opportunities associated with
80 commercial-scale injection of CO₂ into the GHSZ.

2 Methods

PFLOTTRAN's HYDRATE mode was originally developed to model methane generation, transport, and structure 1 (SI) gas hydrate formation in deep marine and Arctic terrestrial reservoirs. PFLOTTRAN's HYDRATE mode has been benchmarked against other reservoir simulators for modelling methane gas production from hydrate reservoirs (White et al., 2020). It has
85 been used to predict shallow gas generation and gas hydrate formation offshore the eastern U.S. (Eymold et al., 2021), to study relationships between gas generation and slope stability along the U.S. Atlantic margin (Carty and Daigle, 2022), and to model gas hydrate accumulation offshore Norway (Frederick et al., 2021). An extension of HYDRATE mode to include salinity coupling was developed to investigate viscous fingering and convective mixing in layered marine sediments during methane hydrate formation over geologic time (Fukuyama et al., 2023). Here, we have redeveloped PFLOTTRAN's HYDRATE mode
90 to optionally consider CO₂ as the working gas; to couple fully implicitly with a new parallel well model; to include a new fully coupled salt mass balance; and to consider variable salinity effects on H₂O-CO₂-NaCl mixtures and the CO₂ hydrate phase boundary.



2.1 Governing Equations

A system of three mass balance equations, one energy balance, and one well equation is now solved fully implicitly in PFLOTRAN's HYDRATE mode. The mass conservation equations take the following form:

$$\frac{\partial}{\partial t} \phi \sum_{\alpha=l,g,h,i,s} (s_{\alpha} \rho_{\alpha} x_j^{\alpha}) + \nabla \cdot (\mathbf{q}_l \rho_l x_j^l + \mathbf{q}_g \rho_g x_j^g - \phi s_l D_l \rho_l \nabla x_j^l - \phi s_g D_g \rho_g \nabla x_j^g) = Q_j + Q_{w,j}, \quad (1)$$

where phase α can be liquid (l), gas (g), hydrate (h), ice (i), or salt precipitate (s); component j includes water, gas (CO₂, CH₄, or air), and salt (NaCl); s_{α} is the saturation of phase α ; ρ_{α} is the density of phase α ; x_j^{α} is the mole fraction of component j in phase α ; q_l is the liquid Darcy flux vector; q_g is the gas Darcy flux vector; D_l is the liquid phase diffusivity; D_g is the gas phase diffusivity; ϕ is the porosity; and Q_j includes any non-well sources/sinks of component j ; and $Q_{w,j}$ is a source/sink of component j from a well. Solid phases are considered immobile and include the hydrate, ice, and salt precipitate phases. Mole fractions of components in the solid phases are fixed: by the hydration number in the hydrate phase, as pure water in the ice phase, and as pure salt in the salt precipitate phase. Formation of gas hydrate and ice therefore results in salt exclusion and aqueous dissolved salinity enhancement, which affects the hydrate phase boundary and gas solubility in the brine.

The energy conservation equation takes the form:

$$\sum_{\alpha=l,g,h,i,s} \left(\frac{\partial}{\partial t} (\phi s_{\alpha} \rho_{\alpha} U_{\alpha}) + \nabla \cdot (\mathbf{q}_{\alpha} \rho_{\alpha} H_{\alpha}) \right) + \frac{\partial}{\partial t} \left((1 - \phi) \rho_r C_p T \right) - \nabla \cdot (\kappa \nabla T) = Q_e + Q_{w,e}, \quad (2)$$

where U_{α} is the internal energy of phase α , H_{α} is the enthalpy of phase α , ρ_r is the rock density, C_p is the heat capacity of the rock, κ is the composite thermal conductivity of the medium, T is the temperature, Q_e includes any non-well heat sources/sinks, and $Q_{w,e}$ is a heat source/sink imposed by the well (e.g., a heater in addition to a fluid injection). Exothermic hydrate formation (and vice versa, i.e., endothermic hydrate dissociation) is captured here by a decrease in internal energy of the hydrate phase during formation; this typically results in either an increase in system temperature or a change in phase saturations in three-phase systems. As we will show later, this phenomenon is important during CO₂ injection in the short term and it can continue to buffer conversion between phases for hundreds of years; similar effects have been shown for natural CH₄ hydrate systems where the base of the gas hydrate stability zone is shifted due to climactic changes (Owulunmi et al., 2022).

A fully implicit, parallel well model has also been incorporated into HYDRATE mode. A well model can more accurately represent the insertion of a (comparably) small cylindrical wellbore into a reservoir grid cell than a standard source/sink term. Given a prescribed surface injection rate of CO₂ into the well, the well model solves for pressure variation along a wellbore



and dynamically adjusts flow rates into the reservoir in response to changes in reservoir physical properties like permeability.
125 This phenomenon can be critical to capture in a horizontal well or injection into a heterogeneous reservoir in the gas hydrate
stability zone, where near-wellbore formation (or dissociation) of gas hydrate can significantly alter reservoir permeability and
thus injection behaviour. The well model developed for HYDRATE mode is a hydrostatic well model based off the design of
White et al. (2013) but with key modifications including full parallelization to run flexibly on very large, unstructured grids
and the addition of a thermal component; as we show here, injection temperature could be one of the most important design
130 considerations for CO₂ storage in the gas hydrate stability zone. The well model developed here accounts for the enthalpy of
the injected CO₂ at the prescribed temperature and wellbore pressure using the same equation of state (EOS) as the reservoir.

Solving a hydrostatic well model involves solving one extra conservation equation per well in addition to the reservoir mass
and energy conservation equations. This means that for one well, only one extra row and one extra column are used in the fully
135 implicit flow Jacobian, *not* an extra row and extra column for each reservoir cell associated with a well. For each reservoir cell
intersected by a well, well pressure is computed at the centroid of the well section crossing through the reservoir. All well
pressures are determined from the bottom hole pressure, a primary variable (see Section 2.3). The well model conservation
equation is compact and reads as follows:

$$140 \quad \sum_i Q_{w,j}^i = q_{w,j}, \quad (3)$$

where i is the discrete reservoir cell index through which the wellbore passes, $Q_{w,j}^i$ are the reservoir source/sink terms of phase
 j associated with a well in reservoir grid cell i , and $q_{w,j}$ is the prescribed surface injection rate of phase j .

2.2 Constitutive Relationships

145 Diffusive flux is modelled using Fick's Law with diffusivities computed as functions of temperature and salinity for CO₂
(Cadogan et al., 2014) and NaCl (Reid et al., 1987). Advective fluxes of mobile phases are computed by employing a two-
phase Darcy's Equation:

$$150 \quad q_\alpha = -\frac{kk_\alpha^r}{\mu_\alpha} \nabla(P_\alpha - \rho_\alpha \mathbf{g}z) \quad (4)$$

where k is the intrinsic medium permeability, k_α^r is the relative permeability of phase α , μ_α is the viscosity of phase α , P_α is
the pressure of phase α , \mathbf{g} is the gravity vector, and z is depth. Relative permeability is computed as a function of phase
 saturations according to one of a suite of standard relative permeability relationships available in PFLOTTRAN. Phase densities
and viscosities are computed as function of temperature, pressure, and salinity according to several options in PFLOTTRAN;



155 for CO₂, the Span-Wagner equation of state is recommended, and for pure water the IF97 equation of state is typically used.
Salt is tracked only in the aqueous phase, and affects brine density (Haas, 1976), viscosity (Phillips et al., 1981), enthalpy, and
diffusivity (Cadogan et al., 2014; Belgodere et al., 2015).

Gas phase pressure and liquid phase pressure are related as a function of gas phase saturation through a choice of capillary
160 pressure functions available in PFLOTRAN. When the gas hydrate phase is present, a capillary pressure associated with the
hydrate phase is computed using the same capillary pressure function as the gas phase, scaled by the ratio of interfacial tension
vis-à-vis Leverett scaling (Leverett, 1941). This capillary pressure is used in the Gibbs-Thomson equation vis-à-vis the Young-
Laplace equation to determine the hydrate 3-phase equilibrium temperature depression required to precipitate hydrate in pores
as follows:

165

$$\Delta T_m = - \frac{T_{mb} P_c}{\Delta H_m \rho_h} \quad (5)$$

where ΔT_m is the change in the hydrate melting temperature, P_c is the hydrate phase capillary pressure, T_{mb} is the bulk melting
temperature, ΔH_m is the specific enthalpy of the phase transition, and ρ_h is the density of solid hydrate. A similar method is
170 often used to compute ice freezing temperature depression vis-à-vis the Clausius-Clapeyron equation. This effect is typically
only significant in fine-grained sediments and/or at very high effective hydrate phase saturations (Anderson et al., 2003).

When both gas hydrate and free gas occupy significant fractions of the pore space, as would be common during CO₂ injection,
their combined presence in the pore system should be accounted for through an effective saturation that is passed to the
175 capillary pressure function. At three-phase (aqueous, free gas/CO₂ phase, gas hydrate) equilibrium, the chemical potential of
CO₂ in the gas hydrate phase at a given hydrate capillary pressure must equal that of CO₂ in the free gas phase at a different
free gas capillary pressure and dissolved CO₂. At bulk thermodynamic equilibrium, free gas and gas hydrate are stable together
at a single pressure and temperature. In porous media, capillary effects on both the hydrate phase and gas phase lead to a
window of possible pressures and temperatures over which three-phase equilibrium can be maintained (Clennell et al., 1999).
180 To incorporate this effect and maintain thermodynamic reversibility, we adopt the approach of Liu and Flemings (2011) and
require free gas and gas hydrate to partition the large pore space equally when both are present (Nole et al., 2018). This
partitioning scheme results in the following effective saturations of free gas and gas hydrate:

185

$$s_{\alpha, \text{eff}} = \begin{cases} 2s_{\alpha}, & s_{\alpha} < s_{\beta} \\ s_{\alpha} + s_{\beta}, & \text{otherwise} \end{cases} \quad (6)$$

where $s_{\alpha, \text{eff}}$ is the effective saturation of nonwetting phase α and β is the other nonwetting phase in a 3-phase system where
liquid water is the wetting phase.



Well flux at each reservoir grid cell is computed as a function of the pressure difference between the well and the reservoir
190 cell (free gas [CO₂] phase pressure for gas injection) scaled by the well index as follows:

$$Q_{w,j} = \frac{WI\rho_j}{\mu_j} (P_w - (P_r + \rho_j g \Delta z_{w-r})) \quad (7)$$

where P_w is the well node pressure, P_r is the reservoir pressure of phase j in the grid cell associated with a given well node,
195 and Δz_{w-r} is the vertical distance between well node centre and reservoir cell centre. The well index, WI , is calculated using a
3D extension of the Peaceman equation incorporating wellbore radius, well skin factor, reservoir directional permeability, and
reservoir grid discretization (White et al., 2013).

The presence of gas hydrate in the pore space of a reservoir decreases the reservoir's permeability below its intrinsic (water-
200 saturated) permeability. We model permeability reduction as a function of hydrate saturation as follows (Dai and Seol, 2014):

$$k_{\text{eff}} = \frac{(1-s_h)^3}{(1+2s_h)^2} \quad (8)$$

where k_{eff} is the effective permeability coefficient and is multiplied by intrinsic permeability to compute the effective absolute
205 permeability.

Heat transfer occurs through mobile fluid phase flow, phase transitions, thermal conduction, and injection/production. Fluid
phase enthalpies are computed using corresponding equations of state. For the CO₂ phase, the Span-Wagner equation of state
is recommended (Span and Wagner, 1996), and for water the IF97 equation of state with salinity extensions are available in
210 PFLOTRAN. Enthalpies of the solid gas hydrate (Handa, 1998) and salt (Lide and Kehiaian, 2020) phases are computed as
functions of temperature. Several options for composite thermal conductivity can be used; the default thermal conductivity
function is a linear scaling function of phase saturations:

$$\kappa = \kappa_{\text{dry}} + \phi \sum_{\alpha=1,g,h,i,s} S_{\alpha} \kappa_{\alpha} \quad (9)$$

215 where κ_{dry} is the dry rock thermal conductivity and κ_{α} is the thermal conductivity of phase α .

The presence of salt has several impacts on system behaviour. If present, salt precipitation reduces permeability, which affects
CO₂ injectivity, gas flow, and liquid imbibition during injection and very far into the future. This occurs either at the injection



220 site if enough CO₂ is injected to dry out the water or far into the future when free phase CO₂ has undergone conversion to very
high hydrate saturations (though at this point, permeability reduction due to salt precipitation is dwarfed by the presence of
solid hydrate at high saturations). Aqueous dissolved salt concentration affects the density of the aqueous phase; the presence
of gradients in salt concentration drives convective mixing. Salt exclusion during hydrate formation locally increases salt
concentrations, which can produce this phenomenon (Fukuyama et al., 2023). Dissolved salt also affects gas solubility and
225 shifts the three-phase equilibrium pressure of gas hydrate. Carbon dioxide equilibrium phase partitioning is computed using
the method of Spycher and Pruess (2010); the CO₂ hydrate – free phase CO₂ – water three-phase equilibrium curve is
determined from a polynomial fit of data from Men et al. (2022) up to the upper quadruple point (283K), beyond which point
a steep line was used to preserve differentiability of the phase boundary.

230 2.3 Phase States and Primary Variables

PFLOTTRAN's HYDRATE mode solves mass conservation, energy conservation, and well flux conservation equations for a
set of three components (CH₄/CO₂/air, H₂O, NaCl) over five phases (aqueous, gas component-rich/gas, gas hydrate, ice, salt
precipitate). This results in solving a set of four partial differential equations for all cells in the domain plus one coupled well
equation per cell containing the bottom segment of a well. Therefore, PFLOTTRAN's fully implicit solution solves for four
235 primary variables everywhere plus one extra primary variable per well in the domain.

The reservoir (non-well) equations use primary variable switching depending on the thermodynamic state of a grid cell.
HYDRATE mode contains 13 phase states with four primary variables per phase state (Table 1). For example, cells in the fully
liquid (aqueous) saturated state solve for liquid pressure, dissolved gas mass fraction, temperature, and total salt mass per unit
240 liquid mass as primary variables. Secondary variables like phase densities, viscosities, and enthalpies are computed at
equilibrium from the primary variables through use of various equations of state. Precipitated salt saturation is computed by
determining whether bulk salt concentration (total salt mass per mass of liquid phase) exceeds dissolved salt solubility and
converting the excess salt mass into a solid phase (permeability updates according to Verma & Pruess [1988]). If dissolved
gas mass fraction exceeds solubility and aqueous pressure, temperature, and dissolved salt mass fraction lie within the GHSZ
245 (i.e., at pressures and temperatures above the 3-phase equilibrium boundary), the cell will transition into the hydrate-aqueous
state and primary variables will update accordingly. Upon entering the hydrate-aqueous state, PFLOTTRAN then switches
primary variables and solves for gas pressure, hydrate saturation, temperature, and salt concentration.

250



Table 1: Phase states and primary variable combinations in PFLOTRAN’s HYDRATE mode

| Phase State | Primary Variables | Phase State | Primary Variables |
|----------------------------|------------------------|--------------------------------|--------------------------|
| L (aqueous) | P_l, x_l^g, T, m_l^s | AI (aqueous-ice) | P_l, x_l^g, S_l, m_l^s |
| G (gas component-rich) | P_g, P_a, T, m_b^s | HGA (hydrate-gas-aqueous) | S_l, S_h, T, m_l^s |
| GA (two-phase gas-aqueous) | P_g, S_g, T, m_l^s | HAI (hydrate-aqueous-ice) | P_g, S_l, S_i, m_l^s |
| HG (hydrate-gas) | P_g, P_a, T, m_b^s | HGI (hydrate-gas-ice) | S_l, S_h, T, m_b^s |
| HA (hydrate-aqueous) | P_g, S_h, T, m_l^s | GAI (gas-aqueous-ice) | P_g, S_g, T, m_l^s |
| HI (hydrate-ice) | P_g, S_h, T, m_b^s | HGAI (hydrate-gas-aqueous-ice) | S_l, S_g, S_i, m_l^s |
| GI (gas-ice) | P_g, S_i, T, m_b^s | | |

P_l = liquid pressure, P_g = gas pressure, P_a = gas-rich gas (air) component partial pressure, x_l^g = aqueous dissolved gas mass fraction, T = temperature, m_l^s = salt mass fraction per unit aqueous mass, m_b^s = total salt mass per unit bulk volume, S_g = gas saturation, S_h = hydrate saturation, S_l = liquid saturation, S_i = ice saturation

255

For the well equation, the bottom hole pressure (BHP) of the well is solved as a primary variable. Given a user-defined well flow rate, each well’s BHP is solved fully implicitly as part of the full reservoir flow solution. At a given BHP, the well model solves for all other pressures in the well by working upward and iteratively solving hydrostatic pressure of the injection fluid where variable fluid density in the well is updated as a function of pressure and temperature. Once the hydrostatic pressures are determined, mass and energy fluxes between well and reservoir at the well segment centroids are computed by adding a hydrostatic adjustment to reservoir pressures to align reservoir pressures with well segment centroids and then employing Equation 7. Fluxes between coupled wells and reservoir cells are therefore functions of the well primary variable (BHP) and reservoir cell primary variables (e.g., gas/liquid pressure).

260

265

Using fully implicit coupling and a Newton-Raphson solution search method, insertion of a coupled well into the domain therefore adds additional fill to the Jacobian matrix used to compute solution updates. Critically, the well model adds extra connectivity beyond the typical stencil for two-point flux calculations. Thus, the structure of the Jacobian matrix is altered by introducing wells. This alteration is typically minimal but would likely become more severe as the number of wells in the domain is increased or as the number of uncased (i.e., screened) segments per well is increased. The number of wells, the extent to which each well increases the fill of the Jacobian, and the strength of the coupling between well and reservoir are all likely to affect the overall performance of simulations using the coupled well model. PFLOTRAN uses neighbour cell ghosting to parallelize computations; the fully coupled well model updates the ghosting stencil to include all off process reservoir cells connected by a given well, allowing for consistent incorporation of well terms in the Jacobian both in parallel and in serial. When a well is turned off (or well flow rates are set to 0), that well equation is not solved.

270



275 3 Results

We demonstrate our developments by applying the software to a set of hypothetical CO₂ injection scenarios in marine environments within the GHSZ. In the first example, liquid CO₂ is injected slowly into a simple 1D homogeneous sediment column through a partially screened well beneath the GHSZ. The second example simulates commercial-scale injection of supercritical CO₂ into a 2D radial domain with heterogeneous layering, where a well is screened within and beneath the GHSZ.
280 The CO₂ plume in this model is tracked for 10,000 years as it transitions from a supercritical phase to a dense liquid phase and then into the gas hydrate phase.

3.1 1D Liquid CO₂ Injection into a Homogeneous Reservoir

In this scenario, a relatively slow trickle injection is designed to illustrate the multiphase and thermodynamic processes associated with injecting CO₂ into the GHSZ. A 1D, 500-m homogeneous domain is initialized to hydrostatic conditions where
285 the top of the domain is held at seafloor pressure of 10 MPa, seafloor temperature of 3° C, and geothermal gradient of 30° C/km. The top Dirichlet boundary condition is set to the initial seafloor temperature, pressure, zero gas mass fraction, and salinity (0.035 kg/kg). The bottom boundary at 500 mbsf is a Neumann zero flux boundary. The domain is discretized into 100 grid cells in the vertical dimension; individual grid cells measure 25 m in the horizontal x-dimension by 1 m in the horizontal
290 y-dimension by 5 m in the vertical z-dimension. A well penetrates the entire domain and is uncased (i.e., screened) for 20 m from 475 meters below seafloor (mbsf) to 495 mbsf. Dense liquid phase CO₂ is injected at 20° C at an injection rate of 5,000 kg/yr for 150 years. Pressure of the injection varies along the well depending on the BHP, but CO₂ remains in the liquid phase for the entirety of the injection. Use of the well model will lead to variable CO₂ injection rates in each of the uncased well segments and correspondingly variable injection enthalpy as a function of well segment pressure; this effect is less noticeable
295 in this homogeneous case than in the heterogeneous case. This simulation is run for 200 years. A constant reservoir porosity is set to 0.35, and constant isotropic permeability is set to 1×10^{-13} m². A Van Genuchten capillary pressure function is used, where Van Genuchten n is set to 1.84162, $\alpha = 0.5$ m⁻¹, and $S_{lr} = 0$. Corey relative permeability functions are used, where $m = 0.457$, $S_{lr} = 0.3$ and $S_{gr} = 0.05$.

300

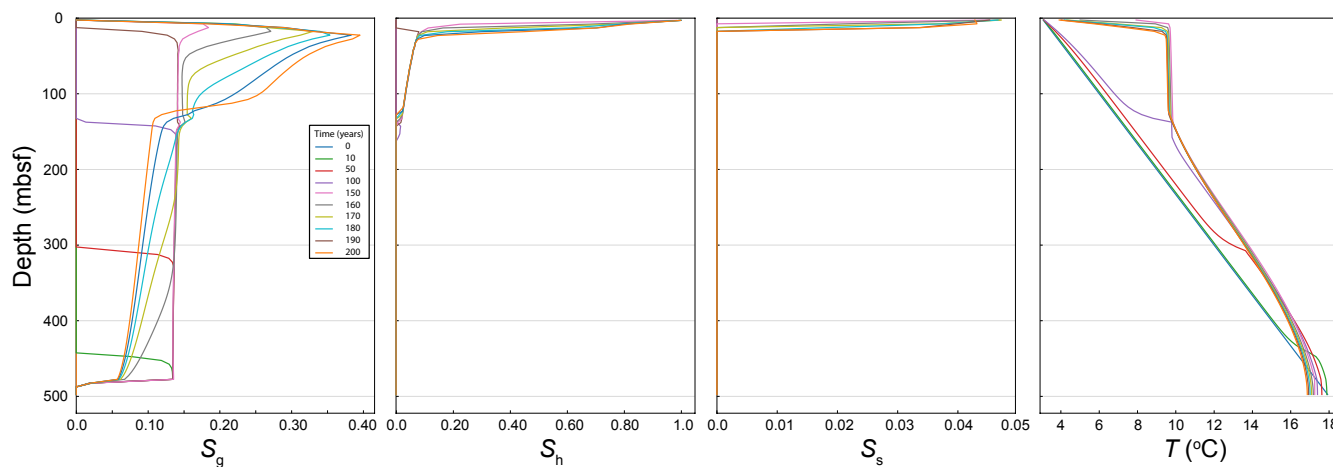


Figure 1: Gas saturation, hydrate saturation, salt precipitate saturation, and temperature during and after a CO₂ injection beneath the GHSZ

305 During the first 50 years of injection, the injected CO₂ remains beneath the base of the CO₂ hydrate stability zone (Figure 1). Therefore, it can only exist as free-phase CO₂. Thus, it migrates upward in characteristic fashion: buoyancy and pressure forces drive gas (free-phase CO₂) saturations exceeding the residual gas saturation to migrate upward in the sediment column. By 100 years, the free-phase CO₂ front has reached the base of the GHSZ. At this point, some free-phase CO₂ converts to CO₂ hydrate. Exothermic hydrate formation keeps the reservoir temperature at the three-phase equilibrium temperature while free-phase CO₂ and hydrate coexist. As the gas plume migrates upward over time, more gas converts into gas hydrate. While the gas supply is strong and hydrate is still forming, the temperature of the reservoir is pushed well above the background (initial) geothermal temperature. CO₂ hydrate cannot form past approximately 10° C, which is why the temperature throughout the three-phase zone is fixed to roughly 10° C.

315 After the injection period ends, hydrate accumulates in high saturations near the top of the domain due to the seafloor temperature and pressure being fixed; the resulting permeability reduction causes gas to pool and salt to concentrate, leading to salt precipitation. This kind of scenario is unlikely to occur in a more realistic reservoir in 2D and 3D where permeability reduction would cause gas to migrate laterally and therefore not cause such significant pooling effects. But this model illustrates how merely relying on conversion of CO₂ to gas hydrate alone as a CO₂ trapping mechanism is likely insufficient due to the thermal buffering effect of exothermic hydrate formation. Permeability reduction associated with gas hydrate formation can act to slow free-phase CO₂ migration, but, at least at early time, a combination of thermodynamic and other structural trapping mechanisms is likely necessary to ensure the long-term sequestration of most of the injected CO₂ in the subsurface GHSZ.

320



3.2 Supercritical CO₂ Injection into a 2D Heterogeneous Reservoir

In this scenario, a commercial-scale CO₂ injection is modelled under more realistic reservoir and injection conditions (Figure 2). A 2D, heterogeneous cylindrical domain extends from the seafloor down to 600 mbsf with a radius of 3.765 km. The model domain consists of 40 grid cells in the horizontal dimension increasing in thickness from 7.38 m at the model centre to 364.36 m at the far edge. The model contains 55 cells in the vertical dimension with varying thickness, each corresponding to a different layer in the model. The model consists of interbedded sand and mud units as might be found within the marine GHSZ. High and low permeability layers alternate with synthetic heterogeneity; similarly, the model contains heterogeneous porosity and capillary entry pressure. All other physical properties are kept constant between layers. A Brooks-Corey capillary pressure function along with Burdine relative permeability functions for liquid and gas phases are used for all layers. For all layers, Brooks-Corey $\lambda = 0.8311$ and $S_{Hl} = S_{rg} = 0.0597$. The capillary entry pressure (the inverse of which is expressed by the Brooks-Corey α parameter) varies between reservoir layers (Figure 3). Rock density is set to 2,650 kg/m³, dry rock thermal conductivity is set at 2.0 W/m-C, and soil compressibility is modelled with a linear compressibility function using a soil compressibility of 1.0E-8 Pa⁻¹ and a reference pressure of 10 MPa. Seafloor pressure is set to 10 MPa, seafloor temperature is 5° C, and seafloor salinity is 0.035 kg/kg. The model is initialized at hydrostatic pressure, constant salinity, and a geothermal gradient of 20° C/km. The top and outer edges of the domain are kept at the initial conditions. The bottom boundary condition is set to no liquid or gas flux, constant salinity, and a constant heat flux to preserve the geothermal gradient.

The well used in this scenario extends from the seafloor to 300 mbsf and is cased for the first 100 m. The rest of the well is uncased; flow from well to reservoir is possible only in the uncased interval. Given the conditions outlined above, the bulk BHSZ for CO₂ hydrate is at approximately 250 mbsf. Therefore, the well in this scenario extends through the GHSZ and 50 m below the bulk BHSZ. Care was taken to ensure that the required well pressures to achieve the specified CO₂ injection rate were realistic; the 100 m depth of well casing was chosen so that the well pressures resulting from our prescribed injection rate did not exceed the lithostatic pressure. This calculation is approximate and does not consider the fracture gradient; the fact that well pressures can easily approach the lithostatic gradient in these settings means that reservoir integrity should be evaluated when performing site-specific evaluations of CO₂ injectivity in the shallow subsurface.

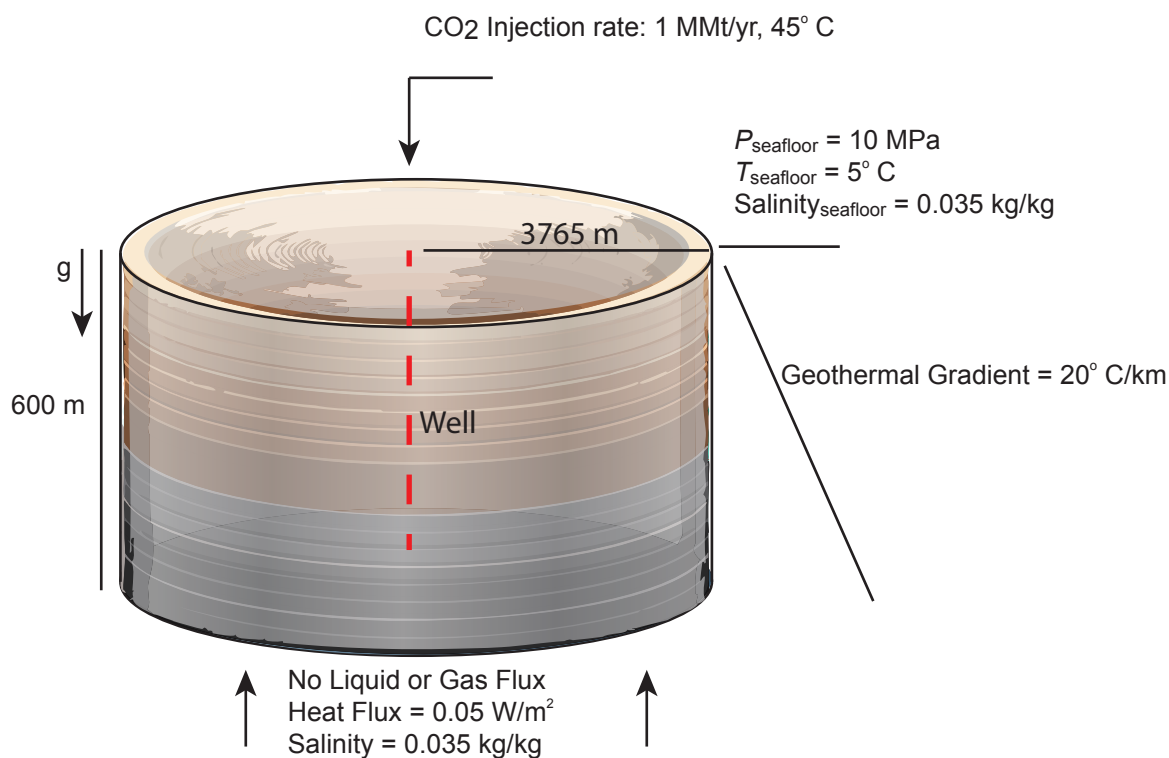


Figure 2: Schematic of the heterogeneous 2D cylindrical model injection scenario

350

The model is run for 10,000 years. The injection is designed as if the reservoir were a prospective DOE CarbonSAFE storage complex. Therefore, CO₂ is injected continuously at a rate of 1 million metric tons (MMT) per year for 50 years to meet a storage target of 50 MMT of CO₂. The CO₂ is injected at a constant temperature of 45° C; injection pressure will vary along the wellbore depending on the hydrostatic pressure of the well, and this in turn will affect the enthalpy of the injected gas.

355 After 50 years, the well is shut off; over time, warm supercritical CO₂ will cool into a dense liquid CO₂ phase and then eventually a gas hydrate phase.

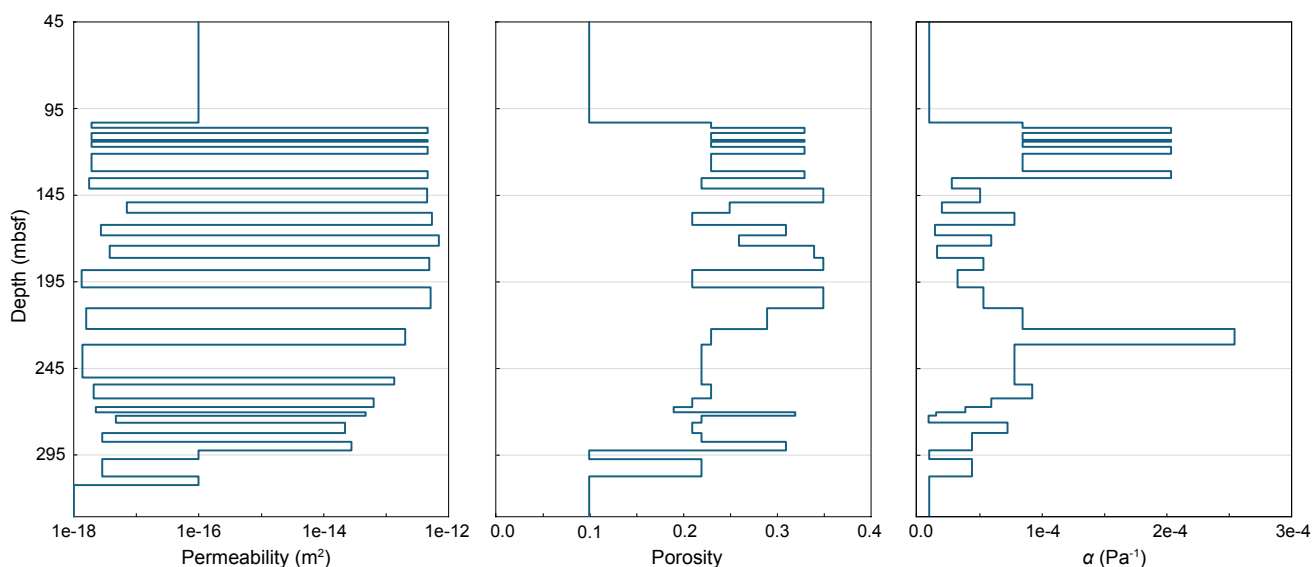
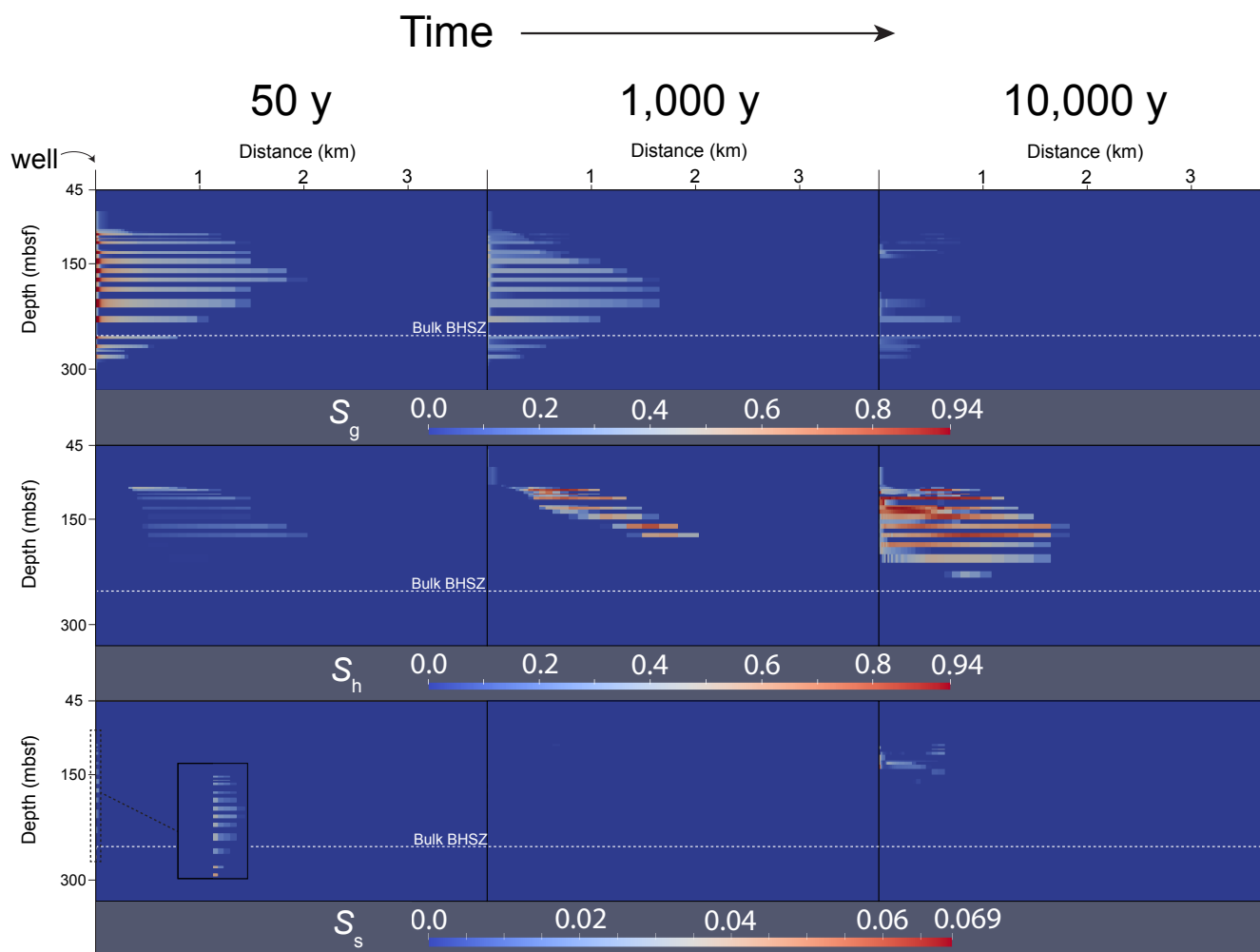


Figure 3: Depth-varying physical properties of the heterogeneous 2D injection scenario, zoomed in near the injection interval.

360 Physical properties held constant above and below these snapshots.

During the 50-year injection interval, gas flows predominantly into the high-permeability reservoir intervals (Figure 4, Figure 5). This is because the well model adjusts the gas flow rate (Figure 6) into individual intervals as a function of hydrostatic well pressure, reservoir pressure, and well index, where well index is a function of reservoir permeability. Since early hydrate
365 formation in the reservoir units elicits a permeability and pressure response, the well flow rate into individual units evolves over time during the injection. In some units, well flow rate drops, and these drops are then compensated by increases in flow rates in other units. Likewise, the pressure in the well evolves over time in response to hydrate formation and relative permeability of the mobile fluids.

370 By the end of the injection period, gas has flowed preferentially in the radial direction along high permeability flow paths. On the outer edges of the gas plume, free phase CO₂ combines with water to form a gas hydrate phase where pressures and temperatures are within the gas hydrate stability zone. Since pure CO₂ is being injected through the well and since water is miscible in the CO₂ phase, high gas saturations in the near-wellbore cells cause salt concentrations in those cells to increase above salt solubility. This salting out effect results in small amounts of salt precipitate saturation in the pore space at the end
375 of the injection.

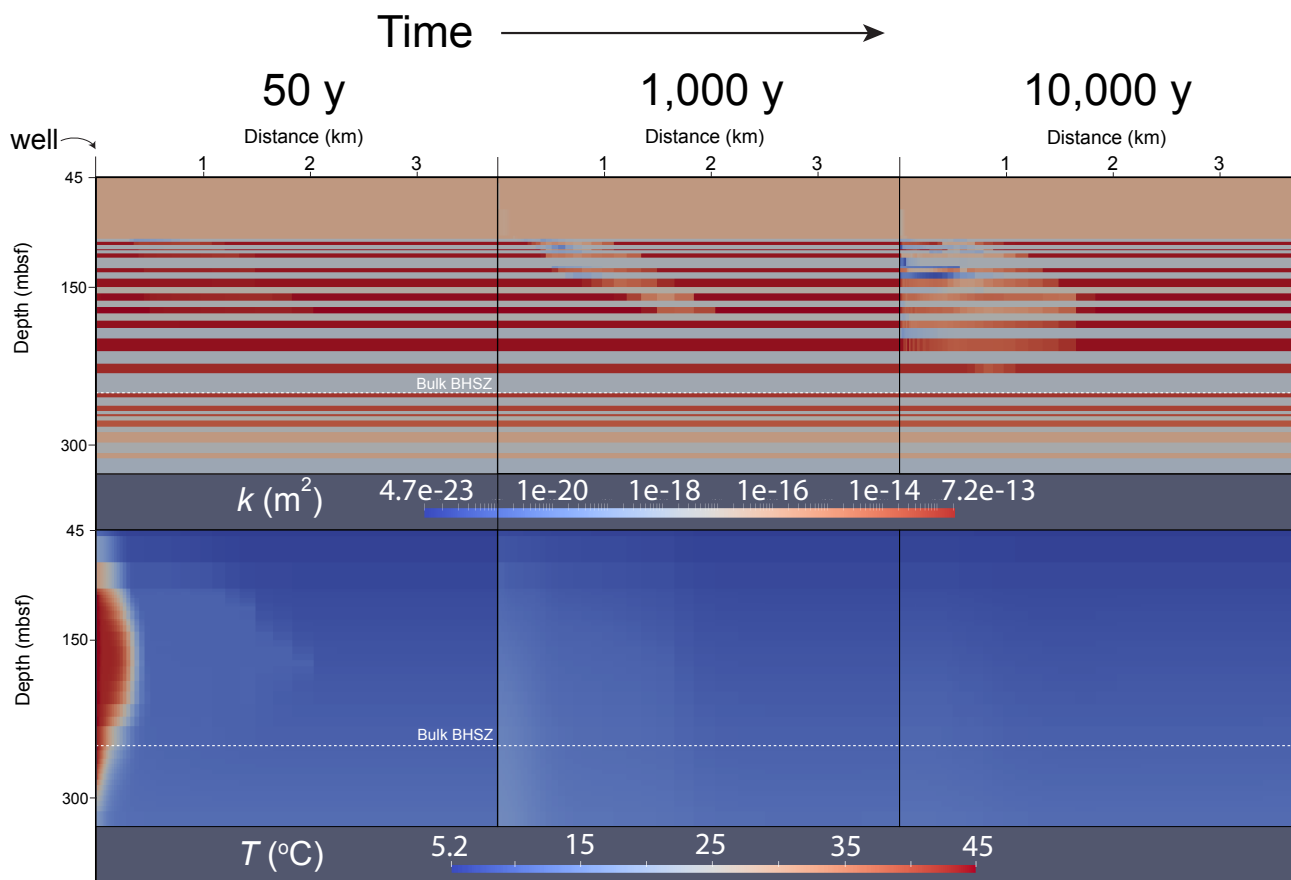


380 **Figure 4:** Snapshots of saturations over time in the vicinity of the wellbore. Depth is represented by the vertical axis, and radial distance from the well is represented by the horizontal axis. Gas (free-phase CO₂) saturation (S_g), hydrate saturation (S_h), and salt precipitate saturation (S_s) distribution at 50 years, 1,000 years, and 10,000 years of simulation time. A zoomed-in cut-out shows near-wellbore salt precipitate saturations at 50 years.

As water imbibes back into the near-wellbore cells between 50 and 1,000 years, gas saturations in those cells drop and salt re-dissolves (salt precipitate saturations near the wellbore drop toward 0). During this time, the temperature of the injected fluid is dropping toward the background temperature field. As this happens, free phase CO₂ combines with available water to form gas hydrate. Exothermic hydrate formation props up temperatures during hydrate formation and slows the process of CO₂ conversion into gas hydrate. In some areas at the upper edges of the CO₂ plume, where the system is furthest into the GHSZ, very high conversion of CO₂ to gas hydrate is achieved in a relatively short amount of time. Since hydrate formation only involves water and CO₂ components, salt exclusion during rapid hydrate formation results in local buildup of salt



390 concentrations. Some cells in the model associated with rapid hydrate formation therefore exhibit some solid salt precipitation
by 1,000 years.



395 **Figure 5: Permeability (k) and temperature (T) distribution at 50 years, 1,000 years, and 10,000 years of simulation time. Depth is
400 represented by the vertical axis, and radial distance from the well is represented by the horizontal axis.**

After 10,000 years, most of the injected CO₂ has converted into gas hydrate. High gas hydrate saturations have built up in the
near-wellbore area since the initial temperature of the injection has decayed away toward the steady-state geothermal
400 temperature profile. Hydrate formation has significantly decreased the permeability of the host reservoir, and gas has migrated
into the other layers to form hydrate. A region of three-phase coexistence (liquid water, free phase CO₂, and gas hydrate) is
still present after 10,000 years because of a combination of exothermic hydrate formation and slow imbibition rates of cool
liquid water due to significant permeability reduction.



405

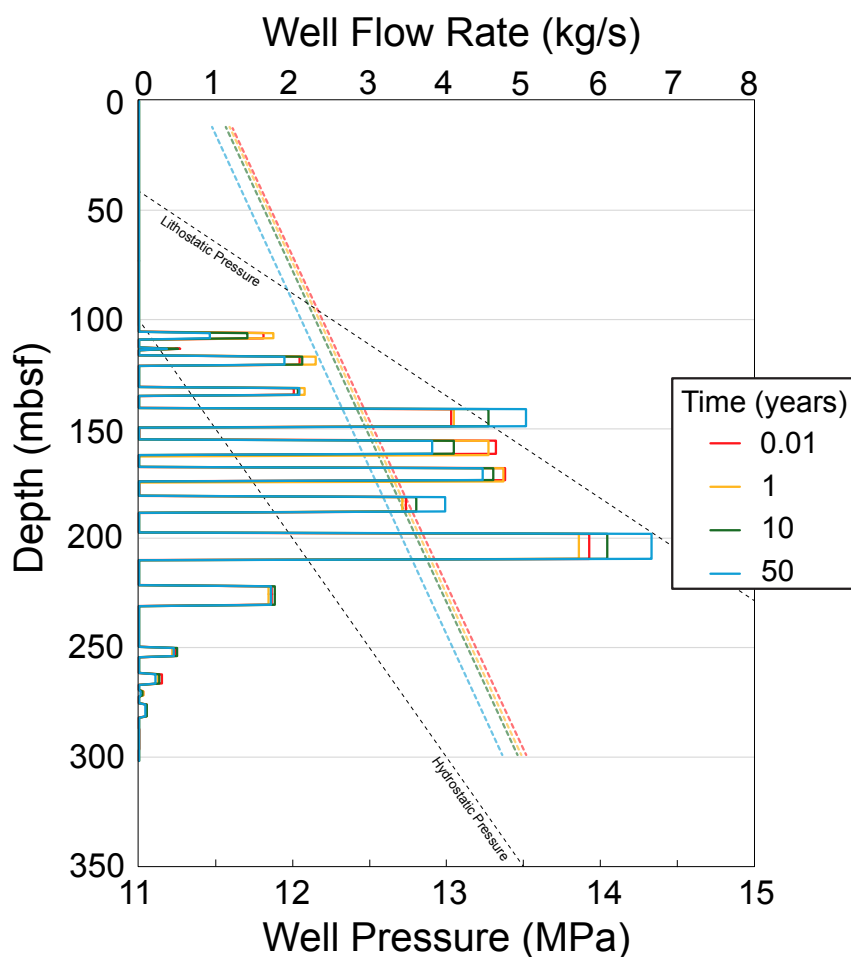


Figure 6: CO₂ mass flow rate in each well segment (solid lines) and supercritical CO₂ phase pressure in the well (dashed lines) during the 50-year injection period.

Discussion

410 The two models presented here were selected to demonstrate some of the key dynamic coupled processes associated with CO₂ injection into the gas hydrate stability zone. In the 1D homogeneous model, CO₂ is injected beneath the GHSZ and forms a free phase which migrates upward due to buoyancy and pressure forces. Once it enters the GHSZ, conversion of CO₂ into an immobile hydrate phase is limited by the rate at which heat can diffuse away and availability of water. When thermal conduction and liquid water flow are limited, the system can maintain 3-phase equilibrium temperature for decades (or
415 thousands of years as is shown in the 2D model). This thermal buffering phenomenon has been observed in models of natural methane hydrate formation and dissociation in marine sediments and can occur on geologic timescales depending on free gas



420 phase flow rate or rate of environmental change (You and Flemings, 2018; Oluwunmi et al., 2022). Clearly, such a scenario would not be ideal for permanent CO₂ sequestration as much of the CO₂ remains in a free phase and accumulates very close to the seafloor. Permeability reduction due to hydrate formation adds a physical trapping mechanism analogous to a low permeability sealing facies. The fact that this permeability reduction is the primary mechanism for preventing CO₂ flow to the surface in the 1D model suggests that physical/structural trapping should be considered just as important or more important than thermodynamic trapping when evaluating a reservoir within the GHSZ for long-term CO₂ storage.

425 The 2D cylindrical model was designed to incorporate more realistic reservoir physical properties and include an injection rate more viable for commercial-scale CO₂ storage in the GHSZ. In this scenario, CO₂ was injected into a layered reservoir that is bounded by low permeability facies that inhibit direct flow of CO₂ to the seafloor. Instead of injecting beneath the GHSZ, a high-temperature supercritical CO₂ phase is injected directly into and directly beneath the GHSZ. Near-wellbore gas hydrate formation is prevented by the high temperature of the injection during the injection period. Hydrate formation does occur during the injection period at the edges of the CO₂ plume; the associated changes in fluid mobility and permeability alter the pressure in the well and cause well flow rates to fluctuate layer-by-layer. Therefore, even if the CO₂ injection temperature is designed to prevent near-wellbore hydrate formation, hydrate formation in the far-field should be considered when designing a CO₂ injection insofar as it could appreciably affect wellbore pressure. Salt precipitation can occur near the wellbore during injection due to “salting out” effects of dry CO₂ injection. Salt can also precipitate later in time as CO₂ converts to hydrate faster than the pore water can freshen through either aqueous imbibition or salt diffusion. In either case, salt precipitate saturations appear to be minimal for the scenario modelled here, but salt precipitation could appreciably decrease permeability under a configuration with either more rapid CO₂ injection or more rapid conversion of CO₂ to hydrate. In some regions of this model, hydrate saturations become very high at late times and lower the permeability of host reservoir units by several orders of magnitude. This makes for effective sealing of CO₂ by conversion to an immobile phase and by impeding flow of the free CO₂ phase. This phenomenon also has the effect of pushing gas into less intrinsically permeable layers and ultimately smoothing the distribution of gas hydrate throughout the model domain.

Conclusions

445 We present several new developments in PFLOTTRAN’s HYDRATE mode including a new option to model CO₂ as the working gas, a new salt mass balance for considering effects of salinity gradients and salt precipitation, and a new fully coupled hydrostatic well model. We demonstrate these new capabilities on a series of test problems designed to explore the coupled processes relevant to CO₂ injection into the marine gas hydrate stability zone for the purpose of permanently sequestering CO₂. CO₂ sequestration in the gas hydrate stability zone is a potentially promising technique for secure storage of CO₂ because of the associated favourable conditions for converting injected CO₂ into solid gas hydrate form, which is immobile in the pore space. However, no reservoir modelling studies to date have demonstrated what commercial-scale CO₂ injection into the gas



hydrate stability zone might look like. We show through a 1D homogeneous model that it is critical to consider multiple
450 trapping mechanisms in addition to the thermodynamic trapping accompanied by conversion of CO₂ into hydrate form. We
then expand to a 2D heterogeneous cylindrical model with a commercial-scale 1 MMT/yr CO₂ injection rate to underscore the
interplay between structural trapping, thermodynamics, and permeability alteration on the migration and conversion of CO₂.
We demonstrate how our fully implicit well model adapts to changes in flow properties during CO₂ injection, and how injection
of a warm supercritical CO₂ phase can facilitate near-wellbore injectivity but can lead to pressure change in the well. In the
455 future, this capability could be used to more rigorously evaluate the potential for secure CO₂ storage in greater volumes, at
larger (3D) scales, with more site-specific inputs, and with more exotic well designs including multiple wells or horizontal
wells.

Code and Data Availability

The software developments described here were released on August 23, 2024 with PFLOTTRAN version 6.0
460 (www.pflotran.org). PFLOTTRAN is open source and freely available under a GNU LGPL Version 3 license at
<https://bitbucket.org/pflotran/pflotran>. Software inputs and a snapshot of the PFLOTTRAN v6.0 Bitbucket repository are
available on Zenodo at <https://zenodo.org/records/13619874>. The files on Zenodo include PFLOTTRAN input decks for both
model scenarios and associated Span-Wagner EOS database files referenced by those input decks.

Acknowledgements

465 This research was supported by the U.S. Department of Energy (DOE) Office of Fossil Energy and Carbon Management and
the National Energy Technology Laboratory (NETL), Award No. FWP 72688. This work was also supported by Pacific
Northwest National Laboratory's (PNNL) Laboratory-Directed Research and Development (LDRD) program, Award No.
211622. PNNL is operated for the DOE by Battelle Memorial Institute under contract DE-AC05-76RL01830. This paper
describes objective technical results and analysis. Any subjective views or opinions that might be expressed in the paper do
470 not necessarily represent the views of the U.S. Department of Energy or the United States Government. Generative AI was
used to develop part of the schematic illustration in Figure 2.

Author Contribution:

MN: software development, model conceptualization, formal analysis, methodology, writing; JB: model conceptualization,
475 writing; FN: model conceptualization, writing; GH: software development, review & editing.

Competing Interests: The authors declare that they have no conflict of interest.



References

- Al Hameli, F., Belhaj, H., & Al Dhuhoori, M. (2022). CO₂ sequestration overview in geological formations: Trapping mechanisms matrix assessment. *Energies*, *15*(20), 7805.
- Anderson, R., Llamedo, M., Tohidi, B., & Burgass, R. W. (2003). Experimental measurement of methane and carbon dioxide clathrate hydrate equilibria in mesoporous silica. *The Journal of Physical Chemistry B*, *107*(15), 3507-3514.
- Belgodere, C., Dubessy, J., Vautrin, D., Caumon, M. C., Sterpenich, J., Pironon, J., ... & Birat, J. P. (2015). Experimental determination of CO₂ diffusion coefficient in aqueous solutions under pressure at room temperature via Raman spectroscopy: impact of salinity (NaCl). *Journal of Raman Spectroscopy*, *46*(10), 1025-1032.
- Cadogan, S. P., Maitland, G. C., & Trusler, J. M. (2014). Diffusion coefficients of CO₂ and N₂ in water at temperatures between 298.15 K and 423.15 K at pressures up to 45 MPa. *Journal of Chemical & Engineering Data*, *59*(2), 519-525.
- Clennell, M. B., Hovland, M., Booth, J. S., Henry, P., & Winters, W. J. (1999). Formation of natural gas hydrates in marine sediments: 1. Conceptual model of gas hydrate growth conditioned by host sediment properties. *Journal of Geophysical Research: Solid Earth*, *104*(B10), 22985-23003.
- Collett, T. S. (2000). Natural gas hydrate as a potential energy resource. In *Natural Gas Hydrate: In Oceanic and Permafrost Environments* (pp. 123-136). Dordrecht: Springer Netherlands.
- Dai, S., & Seol, Y. (2014). Water permeability in hydrate-bearing sediments: A pore-scale study. *Geophysical Research Letters*, *41*(12), 4176-4184.
- Eymold, W. K., Frederick, J. M., Nole, M., Phrampus, B. J., & Wood, W. T. (2021). Prediction of gas hydrate formation at Blake Ridge using machine learning and probabilistic reservoir simulation. *Geochemistry, Geophysics, Geosystems*, *22*(4), e2020GC009574.
- Frederick, J. M., Eymold, W. K., Nole, M. A., Phrampus, B. J., Lee, T. R., Wood, W. T., ... & Conley, E. (2021). *Forecasting marine sediment properties with geospatial machine learning* (No. SAND2021-10675). Sandia National Lab. (SNL-NM), Albuquerque, NM (United States).



- 510 Fu, X., Waite, W. F., & Ruppel, C. D. (2021). Hydrate formation on marine seep bubbles and the implications for water column methane dissolution. *Journal of Geophysical Research: Oceans*, 126(9), e2021JC017363.
- Fukuyama, D., Daigle, H. C., Nole, M. A., & Song, W. (2023). Onset of convection from hydrate formation and salt exclusion in marine sands. *Earth and Planetary Science Letters*, 605, 118039.
- 515 Gauteplass, J., Almenningen, S., Ersland, G., Barth, T., Yang, J., & Chapoy, A. (2020). Multiscale investigation of CO₂ hydrate self-sealing potential for carbon geo-sequestration. *Chemical Engineering Journal*, 381, 122646.
- Goldberg, D., Aston, L., Bonneville, A., Demirkanli, I., Evans, C., Fisher, A., ... & White, S. (2018). Geological storage of
520 CO₂ in sub-seafloor basalt: the CarbonSAFE pre-feasibility study offshore Washington State and British Columbia. *Energy Procedia*, 146, 158-165.
- Haas, J. L. (1976). Physical properties of the coexisting phases and thermochemical properties of the H₂O component in boiling NaCl solution. *Geol. Surv. Bull.*, A, 1421, 73.
- 525 Hammond, G. E., Lichtner, P. C., & Mills, R. T. (2014). Evaluating the performance of parallel subsurface simulators: An illustrative example with PFLOTRAN. *Water resources research*, 50(1), 208-228.
- Handa, Y. P. (1988). A calorimetric study of naturally occurring gas hydrates. *Industrial & engineering chemistry
530 research*, 27(5), 872-874.
- Kaminski, P., Urlaub, M., Grabe, J., & Berndt, C. (2020). Geomechanical behaviour of gassy soils and implications for submarine slope stability: a literature analysis. *Geological Society, London, Special Publications*, 500(1), 277-288.
- 535 Koh, D. Y., Kang, H., Lee, J. W., Park, Y., Kim, S. J., Lee, J., ... & Lee, H. (2016). Energy-efficient natural gas hydrate production using gas exchange. *Applied Energy*, 162, 114-130.
- Lane, J., Greig, C., & Garnett, A. (2021). Uncertain storage prospects create a conundrum for carbon capture and storage ambitions. *Nature Climate Change*, 11(11), 925-936.
- 540 Leverett, M. C. (1941), Capillary behavior in porous solids, *Trans. Am. Inst. Min. Metall. Pet. Eng.*, 142(1), 152-169, doi:10.2118/941152-G.



- 545 Liu, X., & Flemings, P. B. (2011). Capillary effects on hydrate stability in marine sediments. *Journal of Geophysical Research: Solid Earth*, 116(B7).
- Lide, D. R., & Kehiaian, H. V. (2020). *CRC handbook of thermophysical and thermochemical data*. CRC press.
- 550 Men, W., Peng, Q., & Gui, X. (2022). Hydrate phase equilibrium determination and thermodynamic modeling of CO₂+ epoxy heterocycle+ water systems. *Fluid Phase Equilibria*, 556, 113395.
- Nole, M., Daigle, H., Cook, A. E., Malinverno, A., & Flemings, P. B. (2018). Burial-driven methane recycling in marine gas hydrate systems. *Earth and Planetary Science Letters*, 499, 197-204.
- 555 Oluwunmi, P., Pecher, I., Archer, R., Reagan, M., & Moridis, G. (2022). The response of gas hydrates to tectonic uplift. *Transport in Porous Media*, 144(3), 739-758.
- Oyama, A., & Masutani, S. M. (2017). A review of the methane hydrate program in Japan. *Energies*, 10(10), 1447.
- 560 Pang, W., Chen, M., Fu, Q., Ge, Y., Zhang, X., Wen, H., ... & Li, Q. (2024). A Comparative Study of Hydrate-Based CO₂ Sequestration at Different Scales. *Energy & Fuels*.
- Phillips, S. L., Igbene, A., Fair, J. A., Ozbek, H., & Tavana, M. (1981). A technical databook for geothermal energy utilization.
- 565 Rehman, A. N., Bavoh, C. B., Pendyala, R., & Lal, B. (2021). Research advances, maturation, and challenges of hydrate-based CO₂ sequestration in porous media. *ACS Sustainable Chemistry & Engineering*, 9(45), 15075-15108.
- Reid, R. C., Prausnitz, J. M., & Poling, B. E. (1987). *The properties of gases and liquids*.
- 570 Ruppel, C. D., & Kessler, J. D. (2017). The interaction of climate change and methane hydrates. *Reviews of Geophysics*, 55(1), 126-168.
- Singh, R. P., Lall, D., & Vishal, V. (2022). Prospects and challenges in unlocking natural-gas-hydrate energy in India: Recent advancements. *Marine and Petroleum Geology*, 135, 105397.
- 575 Snæbjörnsdóttir, S. Ó., Sigfússon, B., Marieni, C., Goldberg, D., Gislason, S. R., & Oelkers, E. H. (2020). Carbon dioxide storage through mineral carbonation. *Nature Reviews Earth & Environment*, 1(2), 90-102.



- Span, R., & Wagner, W. (1996). A new equation of state for carbon dioxide covering the fluid region from the triple-point
580 temperature to 1100 K at pressures up to 800 MPa. *Journal of physical and chemical reference data*, 25(6), 1509-1596.
- Spycher, N., & Pruess, K. (2010). A phase-partitioning model for CO₂-brine mixtures at elevated temperatures and pressures:
application to CO₂-enhanced geothermal systems. *Transport in porous media*, 82, 173-196.
- 585 Sullivan, M., Rodosta, T., Mahajan, K., & Damiani, D. (2020). An overview of the Department of Energy's CarbonSAFE
Initiative: Moving CCUS toward commercialization. *AIChE Journal*, 66(4), e16855.
- Tohidi, B., Yang, J., Salehabadi, M., Anderson, R., & Chapoy, A. (2010). CO₂ hydrates could provide secondary safety factor
in subsurface sequestration of CO₂. *Environmental science & technology*, 44(4), 1509-1514.
- 590 Verma, A., & Pruess, K. (1988). Thermohydrological conditions and silica redistribution near high-level nuclear wastes
emplaced in saturated geological formations. *Journal of Geophysical Research: Solid Earth*, 93(B2), 1159-1173.
- Wagner, W., & Kretzschmar, H. J. (2008). IAPWS industrial formulation 1997 for the thermodynamic properties of water and
595 steam. *International steam tables: properties of water and steam based on the industrial formulation IAPWS-IF97*, 7-150.
- White, M. D., Bacon, D. H., White, S. K., & Zhang, Z. F. (2013). Fully coupled well models for fluid injection and
production. *Energy Procedia*, 37, 3960-3970.
- 600 White, M. D., Kneafsey, T. J., Seol, Y., Waite, W. F., Uchida, S., Lin, J. S., ... & Zyrianova, M. (2020). An international code
comparison study on coupled thermal, hydrologic and geomechanical processes of natural gas hydrate-bearing
sediments. *Marine and Petroleum Geology*, 120, 104566.
- You, K., & Flemings, P. B. (2018). Methane hydrate formation in thick sandstones by free gas flow. *Journal of Geophysical
605 Research: Solid Earth*, 123(6), 4582-4600.
- Zander, T., Choi, J. C., Vanneste, M., Berndt, C., Dannowski, A., Carlton, B., & Bialas, J. (2018). Potential impacts of gas
hydrate exploitation on slope stability in the Danube deep-sea fan, Black Sea. *Marine and Petroleum Geology*, 92, 1056-1068.